Spin and anomalous Hall effects emerging from topological degeneracy in the Dirac fermion system CuMnAs

Vu Thi Ngoc Huyen,[1] Yuki Yanagi,[1] and Michi-To Suzuki ●[1,2,*]

[1]*Center for Computational Materials Science, Institute for Materials Research, Tohoku University, Sendai, Miyagi 980-8577, Japan*
[2]*Center for Spintronics Research Network, Graduate School of Engineering Science, Osaka University, Toyonaka, Osaka 560-8531, Japan*

Orthorhombic CuMnAs has been proposed as an antiferromagnetic semimetal hosting nodal line and Dirac points around the Fermi level. We investigate relations between the topological bands and transport phenomena, i.e., the spin Hall effect and anomalous Hall effect, in orthorhombic CuMnAs with first-principles calculations combined with a symmetry analysis of the magnetic structures and of the (spin) Berry curvature. We show the nodal line gapped with spin-orbit coupling in CuMnAs dominantly generates large spin Hall conductivity in the ground state. Although the magnetic symmetry in the ground state of CuMnAs forbids the finite anomalous Hall effect, applied magnetic fields produce a significant anomalous component of the Hall conductivity with the magnetic symmetry breaking. We identify that the dominant contribution to anomalous Hall components comes from the further lifting of band degeneracy under external magnetic fields for the Bloch states generated with the splitting of nodal lines by spin-orbit coupling near the Fermi energy.

I. INTRODUCTION

Transport phenomena such as the anomalous Hall effect (AHE) and spin Hall effect (SHE) had been discovered to have a relation to the topological electronic band through the Berry phase theory [1,2]. These phenomena in antiferromagnetic (AFM) systems have essential advantages in comparison with ferromagnetic (FM) systems since there is no unexpected coupling at the interface and no perturbing stray field in the devices due to their magnetization [3].

A large AHE in antiferromagnets has been confirmed experimentally in Mn_3Sn [4] and Mn_3Ge [5], as predicted theoretically in the AFM states in Mn_3Ir [6], Mn_3Sn, and Mn_3Ge [7]. A microscopic mechanism of large AHE is attractive for spintronics applications in enhancing the efficiency or replacing conventional materials. We investigated relations between the energy bands and the large AHE of metallic antiferromagnets Mn_3AN (A = Ni, Cu, Zn, Ga, Ge, Pd, In, Sn, Ir, Pt) in earlier work [8] and identified that the Berry curvature whose size is small but spread widely around the Fermi surfaces in a Brillouin zone (BZ) dominantly contribute to the anomalous Hall conductivity (AHC) rather than the Berry curvature with an extremely large intensity within the local regions around the Weyl points. The presence of large Fermi surfaces thus makes it difficult to distinguish the specific local contribution of topological bands, such as nodal lines and Weyl/Dirac points, to the transport quantities in these metallic magnetic compounds. Therefore, a further investigation of semimetallic magnetic compounds that have only small Fermi surfaces is useful to understand the relation between the topological bands and transport properties in complex magnetic systems,

as was done for the large anomalous Nernst effect of magnetic Weyl semimetals in recent studies of Co_2MnGa and $Co_3Sn_2S_2$ [9–12].

The SHE was theoretically investigated in nonmagnetic compounds as well as magnetic transition metals [13,14] and observed experimentally in metallic AFM compounds PtMn, IrMn, PdMn, and FeMn by highlighting the role of spin-orbit coupling (SOC) to the SHE [15]. The anisotropic property of SHE, i.e., the difference in tensor components of the spin Hall conductivity, in PtMn, IrMn, PdMn, FeMn [15], and $ZrXY$ (X = Si, Ge, Y = S, Se, Te) [16] leads to a possibility to tune a large SHE by exploiting the change in the direction of the electric fields. Besides the electric fields, magnetic fields can control both the SHE and AHE by symmetry breaking. Therefore, an investigation of the origin of SHE and AHE with and without an external magnetic field can pave the way to manipulate the transport phenomena in AFM systems.

The AFM orthorhombic CuMnAs was recently found to be a good candidate for exploring spintronics applications with specific topological features such as topological metal-insulator transitions and topological anisotropic magnetoresistance with the presence of Dirac fermions [17–20]. We further expect that an intensive investigation of the semimetallic magnetic ground state of CuMnAs provides a deeper understanding of the possible contribution from the Bloch states related to the topologically protected degeneracy of the transport phenomena. In this paper, we adopt the semimetallic AFM states of CuMnAs as a platform to investigate the relations between topological bands, such as Dirac/Weyl points and nodal lines, and the transport quantities of SHE and AHE.

The high-symmetric collinear-AFM order of CuMnAs forbids AHC from being finite due to the preserved symmetry of the combined operation of spatial inversion P and time-reversal T. However, as we discuss later, applied magnetic

*mts@tohoku.ac.jp

fields can induce anomalous components of the Hall conductivity by breaking the TP symmetry for the local structure around the nodal line of the electronic bands in the BZ.

The organization of the paper is as follows. Section II presents the method to perform the first-principles calculations and to calculate the spin Hall conductivity (SHC) and anomalous Hall conductivity (AHC). Section III discusses the symmetry aspects of AHE and SHE in CuMnAs with the general relation of the spin Berry curvature. Then, Sec. IV gives computed results about the stability of the AFM structures and their electronic property, along with discussions of the topological bands such as Dirac nodal lines in relation to the AHE and SHE, including the effects of SOC and of external magnetic fields. Finally, Sec. V contains a summary of this work.

II. METHOD

To investigate the relations between specific band structures and transport properties, we study AHE and SHE with the momentum-space Berry phase theory [21,22]. The AHC $\sigma_{\alpha\beta}^{A}$ and SHC $\sigma_{\alpha\beta}^{S,\gamma}$ are evaluated following the Kubo formula [23,24],

$$\sigma_{\alpha\beta}^{A} = -\frac{e^2}{\hbar} \int \frac{d\boldsymbol{k}}{(2\pi)^3} \sum_n f_n(\boldsymbol{k}) \Omega_{n,\alpha\beta}^{A}(\boldsymbol{k}), \tag{1}$$

$$\sigma_{\alpha\beta}^{S,\gamma} = \frac{\hbar}{2e} \frac{e^2}{\hbar} \int \frac{d\boldsymbol{k}}{(2\pi)^3} \sum_n f_n(\boldsymbol{k}) \Omega_{n,\alpha\beta}^{S,\gamma}(\boldsymbol{k}), \tag{2}$$

where n is the band index, $\alpha, \beta, \gamma = x, y, z$ ($\alpha \neq \beta$ for the AHC components), and $f_n(\boldsymbol{k}) = \theta(\mu - \epsilon_{nk})$ is the occupation factor determined from the eigenvalue of the Bloch states ϵ_{nk} and the Fermi energy μ. $\Omega_{n,\alpha\beta}^{A}(\boldsymbol{k})$ and $\Omega_{n,\alpha\beta}^{S,\gamma}(\boldsymbol{k})$ are the Berry curvature and spin Berry curvature, respectively, defined as

$$\Omega_{n,\alpha\beta}^{A}(\boldsymbol{k}) = -2\hbar^2 \,\text{Im} \sum_{m \neq n} \frac{v_{nm,\alpha}(\boldsymbol{k}) v_{mn,\beta}(\boldsymbol{k})}{[\epsilon_m(\boldsymbol{k}) - \epsilon_n(\boldsymbol{k})]^2}, \tag{3}$$

$$\Omega_{n,\alpha\beta}^{S,\gamma}(\boldsymbol{k}) = -\frac{4\hbar}{e} \text{Im} \sum_{m \neq n} \frac{j_{nm,\alpha}^{\gamma}(\boldsymbol{k}) j_{mn,\beta}(\boldsymbol{k})}{[\epsilon_m(\boldsymbol{k}) - \epsilon_n(\boldsymbol{k})]^2}, \tag{4}$$

where the velocity operator is calculated with the periodic part of the Bloch states $u_n(\boldsymbol{k})$ as

$$v_{nm,\alpha}(\boldsymbol{k}) = \frac{1}{\hbar} \left\langle u_n(\boldsymbol{k}) \left| \frac{\partial \hat{H}(\boldsymbol{k})}{\partial k_\alpha} \right| u_m(\boldsymbol{k}) \right\rangle, \tag{5}$$

with $\hat{H}(\boldsymbol{k}) = e^{-i\boldsymbol{k}\cdot\boldsymbol{r}} \hat{H} e^{i\boldsymbol{k}\cdot\boldsymbol{r}}$, $j_\beta = ev_\beta$ is the charge current operator, and $\hat{j}_\alpha^\gamma = \frac{1}{2}\{\hat{s}_\gamma, \hat{v}_\alpha\}$ is the spin-current operator with spin operator s_γ. The (spin) Berry curvature is expected to increase divergently around the band crossing point due to the denominator of Eq. (3) [Eq. (4)]. As a result, the accurate calculation of AHE (SHE) usually requires a dense k mesh for the BZ integration of the (spin) Berry curvature in Eq. (1) [Eq. (2)].

First-principles calculations for magnetic states without an external magnetic field are performed with the QUANTUM ESPRESSO package [25]. The generalized gradient approximation (GGA) in the parametrization of Perdew, Burke, and Ernzerhof [26] is used for the exchange-correlation functional and the pseudopotentials in the projector augmented-wave
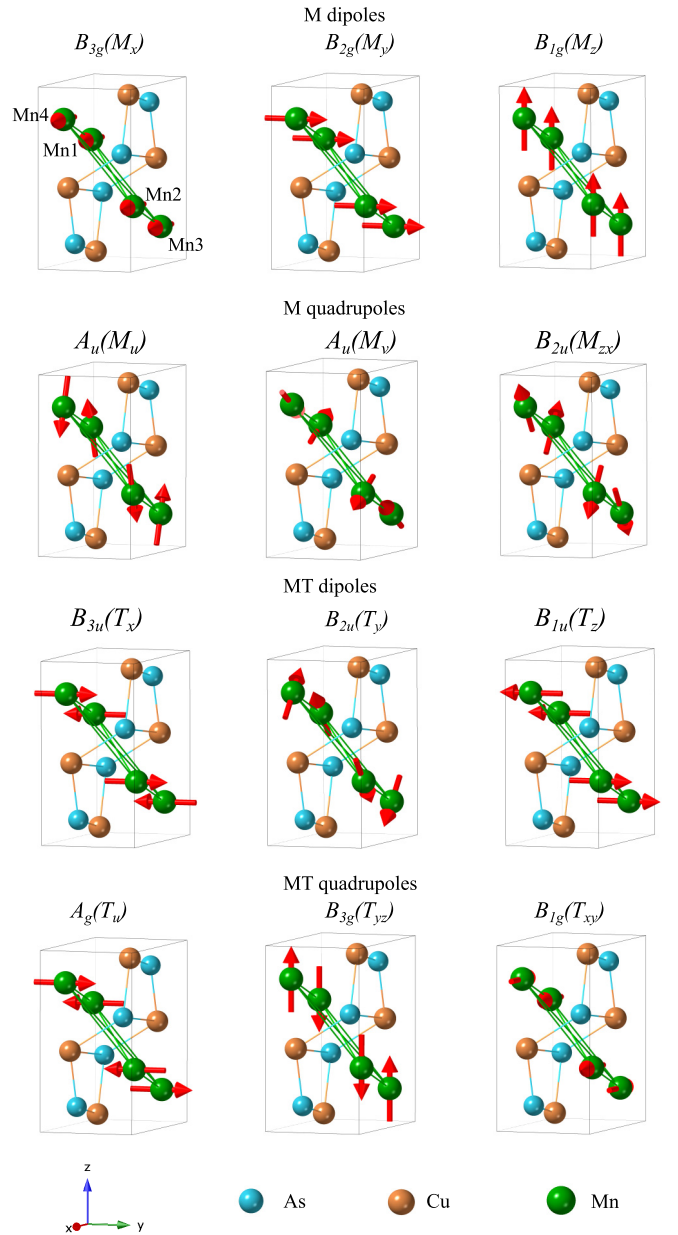

FIG. 1. Energetically inequivalent magnetic structures of CuMnAs classified according to the multipole moments as magnetic (M) dipoles, magnetic (M) quadrupoles, magnetic toroidal (MT) dipoles, and magnetic toroidal (MT) quadrupoles following Ref. [35]. The arrows on Mn atoms indicate the magnetic moments. Four manganese atoms are marked as Mn1, Mn2, Mn3, and Mn4 for $B_{1g}(M_z)$, on which the magnetic alignments are listed in Table I.

method [27,28] are generated by PSLIBRARY [29]. We choose kinetic cutoff energies 50 and 400 Ry for the plane-wave basis set and charge density, respectively. Lattice constants were taken from experimental values [20], which are $a = 6.572$ Å, $b = 3.861$ Å, and $c = 7.305$ Å; the atomic positions are fully relaxed with keeping the lattice constants. A k mesh of $9 \times 15 \times 9$ is utilized to sample the first BZ with a Methfessel-Paxton smearing width of 0.005 Ry to get the Fermi level. The SHC in the absence of an external magnetic field is evaluated with the PAOFLOW package [30].

TABLE I. Classification of the magnetic structures with the ordering vector $\boldsymbol{q} = \boldsymbol{0}$ in CuMnAs according to the symmetry-adapted multipole [35] as well as the irreducible representations (irreps). Magnetic moment alignments for four manganese atoms are listed along with the magnetic space group (MSG), magnetic point group (MPG), and the AHC tensor components (AHC) that can be finite under the magnetic point groups which are also shown in Refs. [36,39].

IREP	Multipole	Magnetic moment alignment			MSG	MPG	AHC
B_{3g}	M_x	Mn1 : 1.0 Mn2 : 1.0 Mn3 : 1.0 Mn4 : 1.0	0.0 0.0 0.0 0.0	0.0 0.0 0.0 0.0	$Pnm'a'$	$m'm'm$	σ_{yz}
B_{2g}	M_y	Mn1 : 0.0 Mn2 : 0.0 Mn3 : 0.0 Mn4 : 0.0	1.0 1.0 1.0 1.0	0.0 0.0 0.0 0.0	$Pn'ma'$	$m'm'm$	σ_{zx}
B_{1g}	M_z	Mn1 : 0.0 Mn2 : 0.0 Mn3 : 0.0 Mn4 : 0.0	0.0 0.0 0.0 0.0	1.0 1.0 1.0 1.0	$Pn'm'a$	$m'm'm$	σ_{xy}
A_u	M_u	Mn1 : −0.410228 Mn2 : −0.410228 Mn3 : 0.410228 Mn4 : 0.410228	0.000000 0.000000 0.000000 0.000000	0.911982 −0.911982 0.911982 −0.911982	$Pn'm'a'$	$m'm'm'$	
A_u	M_v	Mn1 : 0.911982 Mn2 : 0.911982 Mn3 : −0.911982 Mn4 : −0.911982	0.000000 0.000000 0.000000 0.000000	0.410228 −0.410228 0.410228 −0.410228	$Pn'm'a'$	$m'm'm'$	
B_{2u}	M_{zx}	Mn1 : −0.668816 Mn2 : 0.668816 Mn3 : −0.668816 Mn4 : 0.668816	0.000000 0.000000 0.000000 0.000000	−0.743428 −0.743428 0.743428 0.743428	$Pnm'a$	mmm'	
B_{3u}	T_x	Mn1 : 0.0 Mn2 : 0.0 Mn3 : 0.0 Mn4 : 0.0	−1.0 1.0 −1.0 1.0	0.0 0.0 0.0 0.0	$Pn'ma$	mmm'	
B_{2u}	T_y	Mn1 : 0.743428 Mn2 : −0.743428 Mn3 : 0.743428 Mn4 : −0.743428	0.000000 0.000000 0.000000 0.000000	−0.668816 −0.668816 0.668816 0.668816	$Pnm'a$	mmm'	
B_{1u}	T_z	Mn1 : 0.0 Mn2 : 0.0 Mn3 : 0.0 Mn4 : 0.0	1.0 1.0 −1.0 −1.0	0.0 0.0 0.0 0.0	$Pnma'$	mmm'	
A_g	T_u	Mn1 : 0.0 Mn2 : 0.0 Mn3 : 0.0 Mn4 : 0.0	1.0 −1.0 −1.0 1.0	0.0 0.0 0.0 0.0	$Pnma$	mmm	
B_{3g}	T_{yz}	Mn1 : 0.0 Mn2 : 0.0 Mn3 : 0.0 Mn4 : 0.0	0.0 0.0 0.0 0.0	1.0 −1.0 −1.0 1.0	$Pnm'a'$	$m'm'm$	σ_{yz}
B_{1g}	T_{xy}	Mn1 : −1.0 Mn2 : 1.0 Mn3 : 1.0 Mn4 : −1.0	0.0 0.0 0.0 0.0	0.0 0.0 0.0 0.0	$Pn'm'a$	$m'm'm$	σ_{xy}

The ELK code [31] and WANNIER90 [32] are used to investigate the magnetic field dependence of the magnetization, AHE, and SHE under external magnetic fields. The $3p$, $3d$, and $4s$ orbitals of Cu, the $3s$, $3p$, $3d$, and $4s$ orbitals of Mn, the $3d$, $4s$, and $4p$ orbitals of As are treated as band states. The $4s$, $3d$ orbitals for Cu and Mn atoms and $4s$, $4p$ orbitals for As atoms are included for the Wannier interpolation scheme using WANNIER90 to construct the realistic tight-binding models obtained from the first-principles band structures [33]. Most of the AHC and SHC values reach convergence within a few
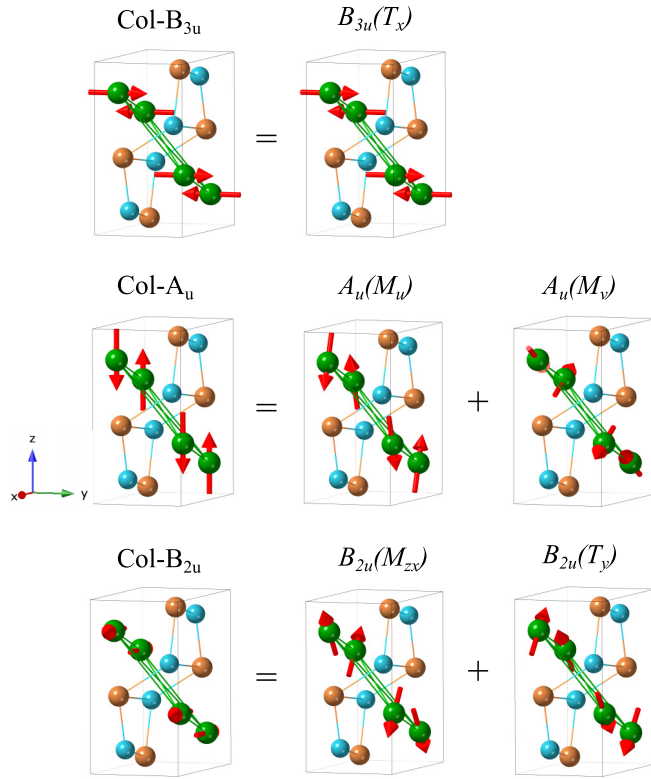
Col-B$_{3u}$ $B_{3u}(T_x)$

Col-A$_u$ $A_u(M_u)$ $A_u(M_v)$

Col-B$_{2u}$ $B_{2u}(M_{zx})$ $B_{2u}(T_y)$

FIG. 2. Linear combinations of the magnetic-structure bases to obtain the collinear-AFM states.

TABLE II. Symmetry operators of magnetic point groups in the Col-B_{3u}, Col-A_u, and Col-B_{2u} structures.

Col-B_{3u}	Col-A_u	Col-B_{2u}
E	E	E
C_{2x}	C_{2x}	C_{2y}
PC_{2y}	C_{2y}	PC_{2x}
PC_{2z}	C_{2z}	PC_{2z}
TC_{2y}	TP	TC_{2x}
TC_{2z}	TPC_{2x}	TC_{2z}
TP	TPC_{2y}	TP
TPC_{2x}	TPC_{2z}	TPC_{2y}

percent under the evaluation with a uniform k-point mesh of $180 \times 280 \times 180$ and an adaptive k-mesh refinement [24,34] of $5 \times 5 \times 5$ for absolute values of the (spin) Berry curvature larger than 100 Å^2. Some calculations, which need a larger k mesh, will be noticed in Sec. IV.

III. SYMMETRY ASPECTS

Orthorhombic CuMnAs crystallizes in the space group *Pnma* (No. 62), whose point group is D_{2h}, and Cu, Mn, and As are all located in the $4c$ site. Figure 1 shows the energetically inequivalent magnetic structures with the ordering vector $\boldsymbol{q} = \boldsymbol{0}$, classified according to the irreducible representations (irreps) of the D_{2h} point group, generated by the cluster multipole expansion scheme of Ref. [35]. The generated magnetic structures are consistent with the decomposition of the magnetic representation $D^{(\mathrm{mag})}$ of the $4c$ site in space group *Pnma* into irreps as follows:

$$D^{(\mathrm{mag})} = A_g \oplus 2B_{1g} \oplus B_{2g} \oplus 2B_{3g}$$
$$\oplus 2A_u \oplus B_{1u} \oplus 2B_{2u} \oplus B_{3u}. \quad (6)$$

We list magnetic moments on four manganese atoms, the magnetic space group, magnetic point groups, and finite AHC tensor components in Table I. The magnetic structures belonging to the ungerade irrep with a subscript u are forbidden to have a finite AHC since they preserve TP symmetry, which imposes the vanishing of the Berry curvature at arbitrary $\boldsymbol{k}$ points in the entire BZ [37,38].

The magnetic toroidal (MT) dipole $B_{3u}(T_x)$ in Fig. 1, corresponding to a collinear AFM with the magnetic moment

orientation along the y axis, was experimentally observed [20]. We refer to this collinear-AFM structure as the Col-B_{3u} structure. The collinear AFM obtained by the linear combination of magnetic (M) quadrupoles M_u and M_v belonging to A_u irrep, referred to as Col-A_u, has local magnetic moments along the z axis. Another collinear AFM obtained by a linear combination of M quadrupole M_{zx} and MT quadrupole T_y belonging to B_{2u} irrep, referred to as Col-B_{2u}, has local magnetic moments along the x axis. Three magnetic structures, Col-B_{3u}, Col-A_u, and Col-B_{2u}, are illustrated in Fig. 2 and their symmetry operators of the magnetic point groups are listed in Table II.

To recognize the finite SHC tensor components as well as to understand the relations of the spin Berry curvature with magnetic symmetry operations, we provide a detailed analysis of the constraint on the spin Berry curvature in k space for some representative symmetries. Considering unitary symmetry operators R and antiunitary symmetry operators $A = TR$ with their representation matrices D^j for the charge current and D^{j_s} for the spin current, respectively, we have relations for the spin Berry curvature for the unitary operation as follows,

$$\Omega_{n,\alpha\beta}^{\mathrm{S},\gamma}(R\boldsymbol{k}) = \sum_{\alpha'\beta'\gamma'} D_{\alpha\gamma\alpha'\gamma'}^{j_s}(R) D_{\beta\beta'}^j(R) \Omega_{n,\alpha'\beta'}^{\mathrm{S},\gamma'}(\boldsymbol{k}), \quad (7)$$

and for antiunitary operation,

$$\Omega_{n,\alpha\beta}^{\mathrm{S},\gamma}(A\boldsymbol{k}) = -\sum_{\alpha'\beta'\gamma'} D_{\alpha\gamma\alpha'\gamma'}^{j_s}(A) D_{\beta\beta'}^j(A) \Omega_{n,\alpha'\beta'}^{\mathrm{S},\gamma'}(\boldsymbol{k}). \quad (8)$$

We list the relations of the reciprocal coordinate $\boldsymbol{k}$ and spin Berry curvature under unitary and antiunitary transformations for some symmetry operations of cubic, tetragonal, and orthorhombic structures in Table III.

As seen in the table, the spin Berry curvature keeps its sign even under the spatial inversion P, the time-reversal T, and TP symmetry. As a result, SHC components can be finite after BZ integration in Eq. (2) even with these symmetries as for the nonmagnetic state. In addition, spin Berry curvature cancels out after BZ integration for most of the components under C_{2x}, C_{2y}, C_{2z}, or in conjunction of these symmetry operators with T, P, or TP, leading to the vanishing of several components of the SHC tensor. For example, we can derive the following

TABLE III. Relations of the reciprocal coordinate $\boldsymbol{k}$ and spin Berry curvature under the unitary and antiunitary transformation for some representative symmetries in the cubic, tetragonal, and orthorhombic systems. $C_{n\mu}$, P, T indicate the n-fold rotation operator along the μ axis, the spatial inversion, and the time-reversal operator, respectively. For example, $\Omega^{S,y}_{yy}$ with [†] in the table means $\Omega^{S,y}_{yy}(\boldsymbol{k}') = \Omega^{S,x}_{xx}(\boldsymbol{k})$ under the C_{4z} symmetry with $\boldsymbol{k}' = (-k_y, k_x, k_z)$.

(a) For $\underline{\boldsymbol{\Omega}}^{S,x}$

$\boldsymbol{k}'=R\boldsymbol{k}$ or $A\boldsymbol{k}$	$\Omega^{S,x}_{xx}$	$\Omega^{S,x}_{xy}$	$\Omega^{S,x}_{xz}$	$\Omega^{S,x}_{yx}$	$\Omega^{S,x}_{yy}$	$\Omega^{S,x}_{yz}$	$\Omega^{S,x}_{zx}$	$\Omega^{S,x}_{zy}$	$\Omega^{S,x}_{zz}$
P	$(-k_x,-k_y,-k_z)$	$\Omega^{S,x}_{xx}$	$\Omega^{S,x}_{xy}$	$\Omega^{S,x}_{xz}$	$\Omega^{S,x}_{yx}$	$\Omega^{S,x}_{yy}$	$\Omega^{S,x}_{yz}$	$\Omega^{S,x}_{zx}$	$\Omega^{S,x}_{zy}$	$\Omega^{S,x}_{zz}$
T	$(-k_x,-k_y,-k_z)$	$\Omega^{S,x}_{xx}$	$\Omega^{S,x}_{xy}$	$\Omega^{S,x}_{xz}$	$\Omega^{S,x}_{yx}$	$\Omega^{S,x}_{yy}$	$\Omega^{S,x}_{yz}$	$\Omega^{S,x}_{zx}$	$\Omega^{S,x}_{zy}$	$\Omega^{S,x}_{zz}$
TP	(k_x,k_y,k_z)	$\Omega^{S,x}_{xx}$	$\Omega^{S,x}_{xy}$	$\Omega^{S,x}_{xz}$	$\Omega^{S,x}_{yx}$	$\Omega^{S,x}_{yy}$	$\Omega^{S,x}_{yz}$	$\Omega^{S,x}_{zx}$	$\Omega^{S,x}_{zy}$	$\Omega^{S,x}_{zz}$
C_{2x}	$(k_x,-k_y,-k_z)$	$\Omega^{S,x}_{xx}$	$-\Omega^{S,x}_{xy}$	$-\Omega^{S,x}_{xz}$	$-\Omega^{S,x}_{yx}$	$\Omega^{S,x}_{yy}$	$\Omega^{S,x}_{yz}$	$-\Omega^{S,x}_{zx}$	$\Omega^{S,x}_{zy}$	$\Omega^{S,x}_{zz}$
C_{2y}	$(-k_x,k_y,-k_z)$	$-\Omega^{S,x}_{xx}$	$-\Omega^{S,x}_{xy}$	$-\Omega^{S,x}_{xz}$	$-\Omega^{S,x}_{yx}$	$-\Omega^{S,x}_{yy}$	$\Omega^{S,x}_{yz}$	$-\Omega^{S,x}_{zx}$	$\Omega^{S,x}_{zy}$	$-\Omega^{S,x}_{zz}$
C_{2z}	$(-k_x,-k_y,k_z)$	$-\Omega^{S,x}_{xx}$	$-\Omega^{S,x}_{xy}$	$\Omega^{S,x}_{xz}$	$-\Omega^{S,x}_{yx}$	$-\Omega^{S,x}_{yy}$	$\Omega^{S,x}_{yz}$	$-\Omega^{S,x}_{zx}$	$\Omega^{S,x}_{zy}$	$-\Omega^{S,x}_{zz}$
$C_{2[1\bar{1}0]}$	$(-k_y,-k_x,-k_z)$	$-\Omega^{S,y}_{yy}$	$-\Omega^{S,y}_{yx}$	$-\Omega^{S,y}_{yz}$	$-\Omega^{S,y}_{xy}$	$-\Omega^{S,y}_{xx}$	$-\Omega^{S,y}_{xz}$	$-\Omega^{S,y}_{zy}$	$-\Omega^{S,y}_{zx}$	$-\Omega^{S,y}_{zz}$
$C_{3[111]}$	(k_z,k_x,k_y)	$\Omega^{S,z}_{zz}$	$\Omega^{S,z}_{zx}$	$\Omega^{S,z}_{zy}$	$\Omega^{S,z}_{xz}$	$\Omega^{S,z}_{xx}$	$\Omega^{S,z}_{xy}$	$\Omega^{S,z}_{yz}$	$\Omega^{S,z}_{yx}$	$\Omega^{S,z}_{yy}$
C_{4z}	$(-k_y,k_x,k_z)$	$\Omega^{S,y}_{yy}[\dagger]$	$-\Omega^{S,y}_{yx}$	$\Omega^{S,y}_{yz}$	$-\Omega^{S,y}_{xy}$	$\Omega^{S,y}_{xx}$	$-\Omega^{S,y}_{xz}$	$\Omega^{S,y}_{zy}$	$-\Omega^{S,y}_{zx}$	$\Omega^{S,y}_{zz}$

(b) For $\underline{\boldsymbol{\Omega}}^{S,y}$

$\boldsymbol{k}'=R\boldsymbol{k}$ or $A\boldsymbol{k}$	$\Omega^{S,y}_{xx}$	$\Omega^{S,y}_{xy}$	$\Omega^{S,y}_{xz}$	$\Omega^{S,y}_{yx}$	$\Omega^{S,y}_{yy}$	$\Omega^{S,y}_{yz}$	$\Omega^{S,y}_{zx}$	$\Omega^{S,y}_{zy}$	$\Omega^{S,y}_{zz}$
P	$(-k_x,-k_y,-k_z)$	$\Omega^{S,y}_{xx}$	$\Omega^{S,y}_{xy}$	$\Omega^{S,y}_{xz}$	$\Omega^{S,y}_{yx}$	$\Omega^{S,y}_{yy}$	$\Omega^{S,y}_{yz}$	$\Omega^{S,y}_{zx}$	$\Omega^{S,y}_{zy}$	$\Omega^{S,y}_{zz}$
T	$(-k_x,-k_y,-k_z)$	$\Omega^{S,y}_{xx}$	$\Omega^{S,y}_{xy}$	$\Omega^{S,y}_{xz}$	$\Omega^{S,y}_{yx}$	$\Omega^{S,y}_{yy}$	$\Omega^{S,y}_{yz}$	$\Omega^{S,y}_{zx}$	$\Omega^{S,y}_{zy}$	$\Omega^{S,y}_{zz}$
TP	(k_x,k_y,k_z)	$\Omega^{S,y}_{xx}$	$\Omega^{S,y}_{xy}$	$\Omega^{S,y}_{xz}$	$\Omega^{S,y}_{yx}$	$\Omega^{S,y}_{yy}$	$\Omega^{S,y}_{yz}$	$\Omega^{S,y}_{zx}$	$\Omega^{S,y}_{zy}$	$\Omega^{S,y}_{zz}$
C_{2x}	$(k_x,-k_y,-k_z)$	$-\Omega^{S,y}_{xx}$	$-\Omega^{S,y}_{xy}$	$\Omega^{S,y}_{xz}$	$-\Omega^{S,y}_{yx}$	$-\Omega^{S,y}_{yy}$	$-\Omega^{S,y}_{yz}$	$\Omega^{S,y}_{zx}$	$-\Omega^{S,y}_{zy}$	$-\Omega^{S,y}_{zz}$
C_{2y}	$(-k_x,k_y,-k_z)$	$\Omega^{S,y}_{xx}$	$-\Omega^{S,y}_{xy}$	$\Omega^{S,y}_{xz}$	$-\Omega^{S,y}_{yx}$	$\Omega^{S,y}_{yy}$	$-\Omega^{S,y}_{yz}$	$\Omega^{S,y}_{zx}$	$-\Omega^{S,y}_{zy}$	$\Omega^{S,y}_{zz}$
C_{2z}	$(-k_x,-k_y,k_z)$	$-\Omega^{S,y}_{xx}$	$-\Omega^{S,y}_{xy}$	$\Omega^{S,y}_{xz}$	$-\Omega^{S,y}_{yx}$	$-\Omega^{S,y}_{yy}$	$-\Omega^{S,y}_{yz}$	$\Omega^{S,y}_{zx}$	$-\Omega^{S,y}_{zy}$	$-\Omega^{S,y}_{zz}$
$C_{2[1\bar{1}0]}$	$(-k_y,-k_x,-k_z)$	$-\Omega^{S,x}_{yy}$	$-\Omega^{S,x}_{yx}$	$-\Omega^{S,x}_{yz}$	$-\Omega^{S,x}_{xy}$	$-\Omega^{S,x}_{xx}$	$-\Omega^{S,x}_{xz}$	$-\Omega^{S,x}_{zy}$	$-\Omega^{S,x}_{zx}$	$-\Omega^{S,x}_{zz}$
$C_{3[111]}$	(k_z,k_x,k_y)	$\Omega^{S,x}_{zz}$	$\Omega^{S,x}_{zx}$	$\Omega^{S,x}_{zy}$	$\Omega^{S,x}_{xz}$	$\Omega^{S,x}_{xx}$	$\Omega^{S,x}_{xy}$	$\Omega^{S,x}_{yz}$	$\Omega^{S,x}_{yx}$	$\Omega^{S,x}_{yy}$
C_{4z}	$(-k_y,k_x,k_z)$	$-\Omega^{S,x}_{yy}$	$\Omega^{S,x}_{yx}$	$-\Omega^{S,x}_{yz}$	$\Omega^{S,x}_{xy}$	$-\Omega^{S,x}_{xx}$	$\Omega^{S,x}_{xz}$	$-\Omega^{S,x}_{zy}$	$\Omega^{S,x}_{zx}$	$-\Omega^{S,x}_{zz}$

(c) For $\underline{\boldsymbol{\Omega}}^{S,z}$

$\boldsymbol{k}'=R\boldsymbol{k}$ or $A\boldsymbol{k}$	$\Omega^{S,z}_{xx}$	$\Omega^{S,z}_{xy}$	$\Omega^{S,z}_{xz}$	$\Omega^{S,z}_{yx}$	$\Omega^{S,z}_{yy}$	$\Omega^{S,z}_{yz}$	$\Omega^{S,z}_{zx}$	$\Omega^{S,z}_{zy}$	$\Omega^{S,z}_{zz}$
P	$(-k_x,-k_y,-k_z)$	$\Omega^{S,z}_{xx}$	$\Omega^{S,z}_{xy}$	$\Omega^{S,z}_{xz}$	$\Omega^{S,z}_{yx}$	$\Omega^{S,z}_{yy}$	$\Omega^{S,z}_{yz}$	$\Omega^{S,z}_{zx}$	$\Omega^{S,z}_{zy}$	$\Omega^{S,z}_{zz}$
T	$(-k_x,-k_y,-k_z)$	$\Omega^{S,z}_{xx}$	$\Omega^{S,z}_{xy}$	$\Omega^{S,z}_{xz}$	$\Omega^{S,z}_{yx}$	$\Omega^{S,z}_{yy}$	$\Omega^{S,z}_{yz}$	$\Omega^{S,z}_{zx}$	$\Omega^{S,z}_{zy}$	$\Omega^{S,z}_{zz}$
TP	(k_x,k_y,k_z)	$\Omega^{S,z}_{xx}$	$\Omega^{S,z}_{xy}$	$\Omega^{S,z}_{xz}$	$\Omega^{S,z}_{yx}$	$\Omega^{S,z}_{yy}$	$\Omega^{S,z}_{yz}$	$\Omega^{S,z}_{zx}$	$\Omega^{S,z}_{zy}$	$\Omega^{S,z}_{zz}$
C_{2x}	$(k_x,-k_y,-k_z)$	$-\Omega^{S,z}_{xx}$	$\Omega^{S,z}_{xy}$	$-\Omega^{S,z}_{xz}$	$\Omega^{S,z}_{yx}$	$-\Omega^{S,z}_{yy}$	$-\Omega^{S,z}_{yz}$	$-\Omega^{S,z}_{zx}$	$-\Omega^{S,z}_{zy}$	$-\Omega^{S,z}_{zz}$
C_{2y}	$(-k_x,k_y,-k_z)$	$-\Omega^{S,z}_{xx}$	$\Omega^{S,z}_{xy}$	$-\Omega^{S,z}_{xz}$	$\Omega^{S,z}_{yx}$	$-\Omega^{S,z}_{yy}$	$-\Omega^{S,z}_{yz}$	$-\Omega^{S,z}_{zx}$	$-\Omega^{S,z}_{zy}$	$-\Omega^{S,z}_{zz}$
C_{2z}	$(-k_x,-k_y,k_z)$	$\Omega^{S,z}_{xx}$	$\Omega^{S,z}_{xy}$	$-\Omega^{S,z}_{xz}$	$\Omega^{S,z}_{yx}$	$\Omega^{S,z}_{yy}$	$-\Omega^{S,z}_{yz}$	$-\Omega^{S,z}_{zx}$	$-\Omega^{S,z}_{zy}$	$\Omega^{S,z}_{zz}$
$C_{2[1\bar{1}0]}$	$(-k_y,-k_x,-k_z)$	$-\Omega^{S,z}_{yy}$	$-\Omega^{S,z}_{yx}$	$-\Omega^{S,z}_{yz}$	$-\Omega^{S,z}_{xy}$	$-\Omega^{S,z}_{xx}$	$-\Omega^{S,z}_{xz}$	$-\Omega^{S,z}_{zy}$	$-\Omega^{S,z}_{zx}$	$-\Omega^{S,z}_{zz}$
$C_{3[111]}$	(k_z,k_x,k_y)	$\Omega^{S,y}_{zz}$	$\Omega^{S,y}_{zx}$	$\Omega^{S,y}_{zy}$	$\Omega^{S,y}_{xz}$	$\Omega^{S,y}_{xx}$	$\Omega^{S,y}_{xy}$	$\Omega^{S,y}_{yz}$	$\Omega^{S,y}_{yx}$	$\Omega^{S,y}_{yy}$
C_{4z}	$(-k_y,k_x,k_z)$	$\Omega^{S,z}_{yy}$	$-\Omega^{S,z}_{yx}$	$\Omega^{S,z}_{yz}$	$-\Omega^{S,z}_{xy}$	$\Omega^{S,z}_{xx}$	$-\Omega^{S,z}_{xz}$	$\Omega^{S,z}_{zy}$	$-\Omega^{S,z}_{zx}$	$\Omega^{S,z}_{zz}$

relations under C_{2x}, PC_{2x}, TC_{2x}, or TPC_{2x} symmetries:

$$\sigma^{S,x}_{xy} = \sigma^{S,x}_{yx} = \sigma^{S,x}_{xz} = \sigma^{S,x}_{zx} = 0,$$

$$\sigma^{S,y}_{xx} = \sigma^{S,y}_{yy} = \sigma^{S,y}_{zz} = \sigma^{S,y}_{yz} = \sigma^{S,y}_{zy} = 0, \qquad (9)$$

$$\sigma^{S,z}_{xx} = \sigma^{S,z}_{yy} = \sigma^{S,z}_{zz} = \sigma^{S,z}_{yz} = \sigma^{S,z}_{zy} = 0.$$

Further finite SHC components can be seen from transformation relations of the spin Berry curvature for other symmetry operations listed in Table III. As the result, from the above symmetry analysis for symmetry operators in Table II, we obtain SHC tensor components finite for the Col-B_{3u}, Col-A_u, and Col-B_{2u} magnetic structures in Table IV, which is consistent with the results shown in Ref. [39].

IV. RESULTS

A. Magnetic stability and ground state properties

We calculate the total energies for the magnetic configurations in Figs. 1 and 2 in the presence of SOC to evaluate the stability of the magnetic structures in the way suggested

TABLE IV. The symmetry-imposed shapes of the SHC tensors for the Col-B_{3u}, Col-A_u, and Col-B_{2u} structures.

$\underline{\sigma}^{S,x}$			$\underline{\sigma}^{S,y}$			$\underline{\sigma}^{S,z}$		
$\begin{pmatrix} 0 \\ 0 \\ 0 \end{pmatrix}$	$\begin{pmatrix} 0 \\ 0 \\ \sigma^{S,x}_{zy} \end{pmatrix}$	$\begin{pmatrix} 0 \\ \sigma^{S,x}_{yz} \\ 0 \end{pmatrix}$	$\begin{pmatrix} 0 \\ 0 \\ \sigma^{S,y}_{zx} \end{pmatrix}$	$\begin{pmatrix} 0 \\ 0 \\ 0 \end{pmatrix}$	$\begin{pmatrix} \sigma^{S,y}_{xz} \\ 0 \\ 0 \end{pmatrix}$	$\begin{pmatrix} 0 \\ \sigma^{S,z}_{yx} \\ 0 \end{pmatrix}$	$\begin{pmatrix} \sigma^{S,z}_{xy} \\ 0 \\ 0 \end{pmatrix}$	$\begin{pmatrix} 0 \\ 0 \\ 0 \end{pmatrix}$

TABLE V. Total magnetization $|M_{\text{total}}|(\mu_B)$ of magnetic structures in Figs. 1 and 2 and the difference in total energy between each magnetic ordering and nonmagnetic state ΔE_{nm} (meV/u.c.) are listed. To easily discern, the different energies ΔE (meV/u.c.) between each magnetic ordering with the most stable magnetic structure Col-B_{2u} are also shown in the last column.

Structure	$|M_{\text{total}}|(\mu_B)$	ΔE_{nm} (meV/u.c.)	ΔE (meV/u.c.)
$B_{3g}(M_x)$	16.3	−3878.5	912.4
$B_{2g}(M_y)$	16.3	−3878.3	912.6
$B_{1g}(M_z)$	16.3	−3878.2	912.7
$A_u(M_u)$	0.0	−4784.3	6.6
$A_u(M_v)$	0.0	−4444.6	346.3
$B_{2u}(M_{zx})$	0.0	−4771.5	19.4
Col-B_{2u}	0.0	−4790.9	0.0
Col-B_{3u}	0.0	−4790.7	0.2
Col-A_u	0.0	−4790.5	0.4
$B_{2u}(T_y)$	0.0	−4784.9	6.0
$B_{1u}(T_z)$	0.0	−4516.7	272.2
$A_g(T_u)$	0.0	−4750.9	40.0
$B_{3g}(T_{yz})$	0.0	−4750.7	40.2
$B_{1g}(T_{xy})$	0.0	−4750.8	40.1

TABLE VI. Relaxed atomic positions for the Col-B_{3u} magnetic structure in CuMnAs.

Atoms	x	y	z
Cu	0.379	0.25	0.055
Cu	0.621	0.75	0.945
Cu	0.121	0.75	0.555
Cu	0.879	0.25	0.445
Mn1	0.457	0.25	0.674
Mn2	0.543	0.75	0.327
Mn3	0.043	0.75	0.174
Mn4	0.957	0.25	0.827
As	0.761	0.25	0.127
As	0.239	0.75	0.873
As	0.739	0.75	0.627
As	0.261	0.25	0.373

recently [40], setting a fully polarized valence state as the initial setting. The obtained total energy differences and total magnetization are listed in Table V. The magnetic structures different only from magnetic anisotropy produce energy differences only by considering SOC and have the same total energies if the first-principles calculations are implemented without SOC. As a result, the Col-B_{2u}, Col-B_{3u}, and Col-A_u structures have close total energies as well as those for the FM structures M_x, M_y, and M_z in Fig. 1 due to the small SOC in the Mn 3d orbitals, as shown in Table V.

The result in Table V shows that Col-B_{2u}, Col-B_{3u}, and Col-A_u are stable structures with an energy difference within 0.4 meV and much lower than other magnetic structures. The small discrepancy of the most stable magnetic structure from the experimentally observed one, that is the calculation predicting the most stable magnetic structure as Col-B_{2u} against the Col-B_{3u} reported in experiment [20], can be addressed to the low accuracy for magnetic anisotropy within GGA calculations [41]. Hereinafter, we will focus on the characteristics of the Col-B_{3u}, Col-A_u, and Col-B_{2u} magnetic structures. The magnetic moments after getting convergence for the calculations using an initial magnetic structure of Col-A_u and Col-B_{2u} have magnetic moments that are slightly canted along the x and z directions, respectively, while those for Col-B_{3u} are purely on the y direction. The difference in the canting structure of magnetic alignments for different collinear-AFM structures is understood from the geometrical degree of freedom of the magnetic alignment adopted in each irrep as illustrated in Fig. 2. The atomic positions obtained for the Col-B_{3u} structure are listed in Table VI, and differences of those for the Col-A_u and Col-B_{2u} structures are within 0.005 Å.

The BZ of orthorhombic CuMnAs is illustrated with high-symmetry points in Fig. 3(a). Figure 3(b) shows the projected density of states for the Col-B_{3u} structure as those for the Col-A_u and Col-B_{2u} structures are similar with the plotted energy

scale. All three collinear-AFM structures are semimetallic and the Mn 3d and Cu 3d orbitals give a large density near the Fermi level, implying their dominant role in the transport properties. The energy bands of tight-binding models reproduce the energy bands obtained by first-principles calculations within the energy interval from the lowest energy of the valence bands to 2 eV above the Fermi energy, as shown in Fig. 3(c).

Figures 4(a), 4(c), 4(e), and 4(g) show the electronic band structures near the Fermi energy in the nonmagnetic, Col-B_{3u} magnetic, Col-A_u magnetic, and Col-B_{2u} magnetic structures plotted both with and without SOC. These collinear-AFM states are characterized with, at least, doubly degenerate electronic bands at all k points due to the preservation of TP symmetry. As a result, crossing points in the energy bands are Dirac points, which are characterized by fourfold band degeneracy. For the calculations neglecting SOC, these collinear-AFM structures have Dirac nodal lines in the (010) plane containing the Γ point as illustrated in Fig. 6(a) with a small dispersion in the energy from 0 to about 30 meV. The nodal line degeneracy for the Col-B_{3u} and Col-B_{2u} magnetic structures splits entirely by considering the effect of SOC. Meanwhile, the Col-A_u magnetic structure forms one pair of Dirac points, protected by screw rotation symmetry S_{2z}, on the nodal line even after considering the SOC, as investigated in Ref. [17]. The two Dirac points of the Col-A_u magnetic structure are located between the X and U points with the coordinates $D_1(0.50, 0.0, 0.47)$ and $D_2(−0.50, 0.0, −0.47)$ at −12.7 meV from the Fermi level.

B. Topological degeneracy and spin Hall effect

Figures 4(b), 4(d), 4(f), and 4(h) show the SHC as a function of chemical potential for the nonmagnetic, Col-B_{3u} magnetic, Col-A_u magnetic, and Col-B_{2u} magnetic structures. The result in the nonmagnetic calculation shows an approximate antisymmetry for SHC components $\sigma_{\alpha\beta}^{S,\gamma} \approx -\sigma_{\beta\alpha}^{S,\gamma}$, while collinear-AFM states exhibit a large anisotropic SHE. We illustrate an example of this anisotropy in Fig. 5. Under electric fields along the x and y direction, we have $\sigma_{xy}^{S,z} \approx -\sigma_{yx}^{S,z}$ for the nonmagnetic state and $|\sigma_{xy}^{S,z}| \gg |\sigma_{yx}^{S,z}|$ for the Col-B_{3u} state. It implies that the spin current flowing along
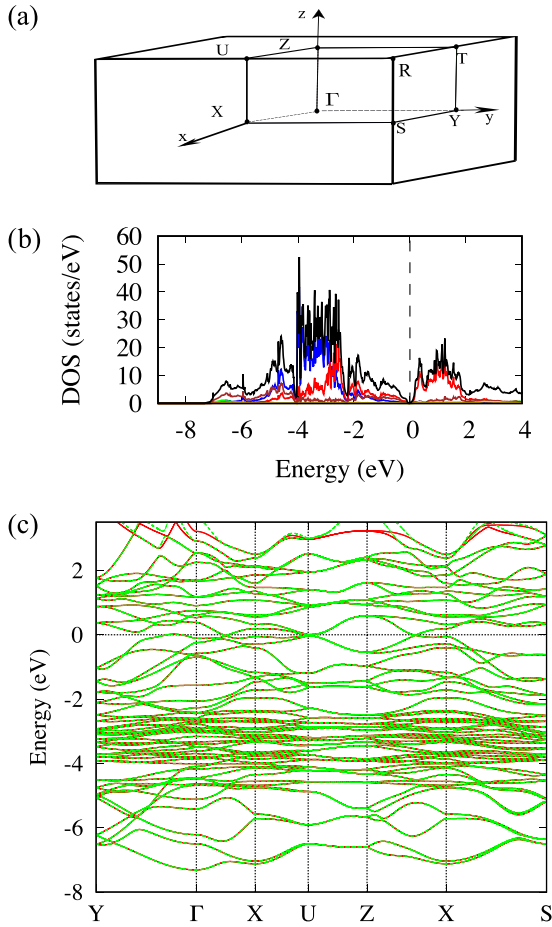
FIG. 3. (a) The first BZ of a simple orthorhombic lattice with high-symmetry points. (b) The projected density of states of the Col-B_{3u} structure for the orbitals Cu 4s (green), Cu 3d (blue), Mn 4s (pink), Mn 3d (red), As 4p (brown), As 4s (gold), and total density of states (black). (c) Energy bands from the first-principles calculations (red) and from a Wannier interpolation (green) of the Col-B_{3u} magnetic structure along high-symmetry lines.

the x direction with the z-spin component is significantly enhanced under an applied electric field along the y direction, i.e., $|j_{x,\text{Col-B}_{3u}}^{S,z}| \gg |j_{x,\text{nonmag}}^{S,z}|$, with the transition from a nonmagnetic state to the AFM state occurring by lowering the temperature. The drastic change of the SHC components by magnetic ordering might be useful for spintronics applications such as to control the spin current by varying the temperature.

The largest components $\sigma_{xy}^{S,z}$ at zero energy have magnitudes of 142.4, 182.0, and 140.8 ($\hbar/e$) S/cm in the Col-B_{3u}, Col-A_u, and Col-B_{2u} magnetic structures, respectively. Each collinear-AFM state has a peak for $\sigma_{xy}^{S,z}$ located near the energy of the Dirac points and nodal line, which is from 0 to about 30 meV below the Fermi energy. A strong dependence on the chemical doping of the SHC is expected from the peak structure of the chemical potential dependence of the SHC around the Fermi level, whose maximum is ~250 ($\hbar/e$) S/cm, which is comparable with first-principles calculation results of ordinary metals such as Ta and W, ~200 ($\hbar/e$) S/cm [13].

Figure 6(b) shows the spin Berry curvature after taking the band summation, $\Omega_{xy,\text{sum}}^{S,z} = \sum_n f_n \Omega_{n,xy}^{S,z}$, integrated over (010) planes with the center changing from $-Y$ to Γ and
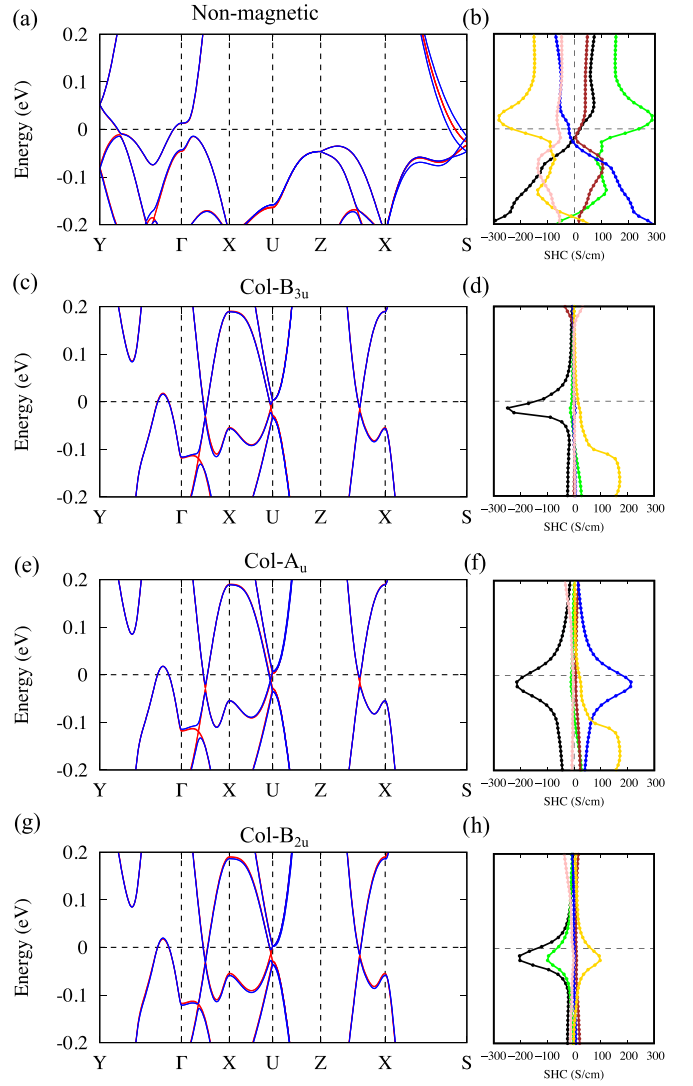

FIG. 4. (a), (c), (e), and (g) Electronic band structures along high-symmetry lines without SOC (red) and with SOC (blue) in (a) nonmagnetic, (c) Col-B_{3u}, (e) Col-A_u, and (g) Col-B_{2u} states, respectively. (b), (d), (f), and (h) The SHC components $\sigma_{xy}^{S,z}$ (black), $\sigma_{yx}^{S,z}$ (blue), $\sigma_{yz}^{S,x}$ (green), $\sigma_{zy}^{S,x}$ (gold), $\sigma_{zx}^{S,y}$ (brown), and $\sigma_{xz}^{S,y}$ (pink) in (b) nonmagnetic, (d) Col-B_{3u}, (f) Col-A_u, and (h) Col-B_{2u} structures, respectively.

to Y in the BZ. The plot shows that the largest contribution from the (010) plane includes the Γ point and reduces with the plane center moving apart from Γ along the y axis. Figures 6(c)–6(e) show the distribution of $\Omega_{xy,\text{sum}}^{S,z}$, which contributes to the SHC $\sigma_{xy}^{S,z}$, in the (010) plane containing the Γ point within the first BZ, illustrated in Fig. 6(a). The plot shows the large $\Omega_{xy}^{S,z}$ distributed around the gapped nodal line, implying the large contribution to the SHC from the Bloch states around the nodal line gapped out with the SOC in the (010) plane. The distribution of the spin Berry curvature in k space must reflect the symmetry constraint from the magnetic point group of the magnetic structure as discussed in Sec. III. As a result, under the mirror symmetry $m_y = PC_{2y}$ and the two-fold rotation C_{2y}, the symmetry of $\Omega_{xy,\text{sum}}^{S,z}$ in Fig. 6(b) for the Col-B_{3u} and Col-A_u structure, respectively, is reflected as

Non-magnetic state $(T > T_C)$

$\sigma^{S,z}_{xy} \approx -\sigma^{S,z}_{yx}$

Col-B_{3u} AFM state $(T < T_C)$
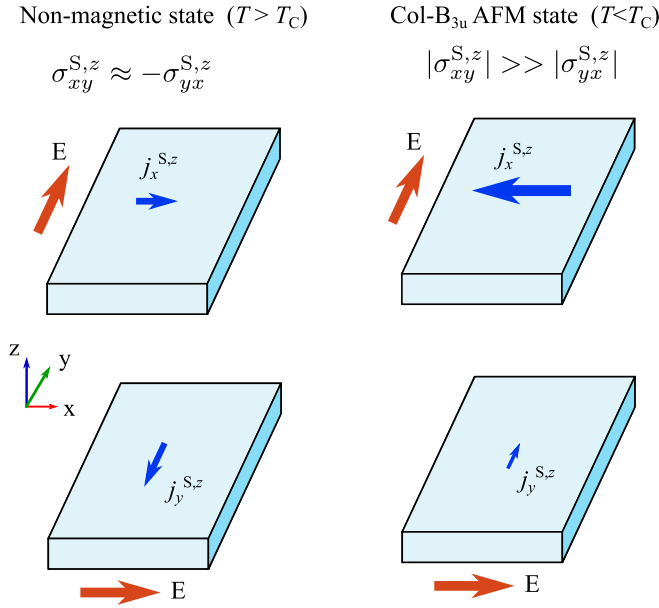
$|\sigma^{S,z}_{xy}| \gg |\sigma^{S,z}_{yx}|$

FIG. 5. Illustration of the anisotropic SHE, which can be exploited for spintronics applications. Here, E is the electric field, $j^{S,z}$ indicates the spin current with a z-spin component, and T_C is the transition temperature from the AFM state to the nonmagnetic state.

$\int \Omega^{S,z}_{xy,\text{sum}}(k_x, -k_y, k_z) dS = \int \Omega^{S,z}_{xy,\text{sum}}(k_x, k_y, k_z) dS$. In Figs. 6(c) and 6(e) the spin Berry curvatures of the Col-B_{3u} and Col-B_{2u} magnetic structures hold the relation $\Omega^{S,z}_{xy,\text{sum}}(k_x, k_y, -k_z) = \Omega^{S,z}_{xy,\text{sum}}(k_x, k_y, k_z)$ with the mirror symmetry $m_z = PC_{2z}$.

C. Spin Hall effect under external magnetic fields

We consider the Col-B_{3u} magnetic structure, which corresponds to the experimentally observed magnetic structure, under applied magnetic fields along the x, y, z directions, H_x, H_y, and H_z. We illustrate the canting of the magnetic direction of Col-B_{3u} under external magnetic fields along the z axis, H_z, in Fig. 7(a). When the external magnetic fields are perpendicular to the direction of the local magnetic moment, the absolute value of net magnetization increases with increasing the magnetic fields as shown in Fig. 7(b) for the magnetic fields H_x and H_z. The external magnetic fields parallel to the local magnetic moments require a large field strength to flip the magnetic moments by conquering the AFM-exchange energy. The large spin-flip transition from AFM to FM corresponding to the energy difference between the two magnetic ordered states shown in Table V prevents magnetization from developing with the applied magnetic fields along the y axis, H_y, as seen in Fig. 7(b). As a result, applying the magnetic field H_y does not affect the SHC in the Col-B_{3u} structure within the investigated range of the magnetic fields in this work.

Figure 7(c) shows the SHC $\sigma^{S,z}_{xy}$ under the magnetic fields applied along the x and z axis for the Col-B_{3u} structure. The absolute value of the SHC reduces with increasing the external magnetic fields, and then it mostly reaches a saturation value when the external magnetic fields increase in the limit of the considered applied magnetic fields from 0 to 85.75 T. We plot the electronic band structure and corresponding spin Berry
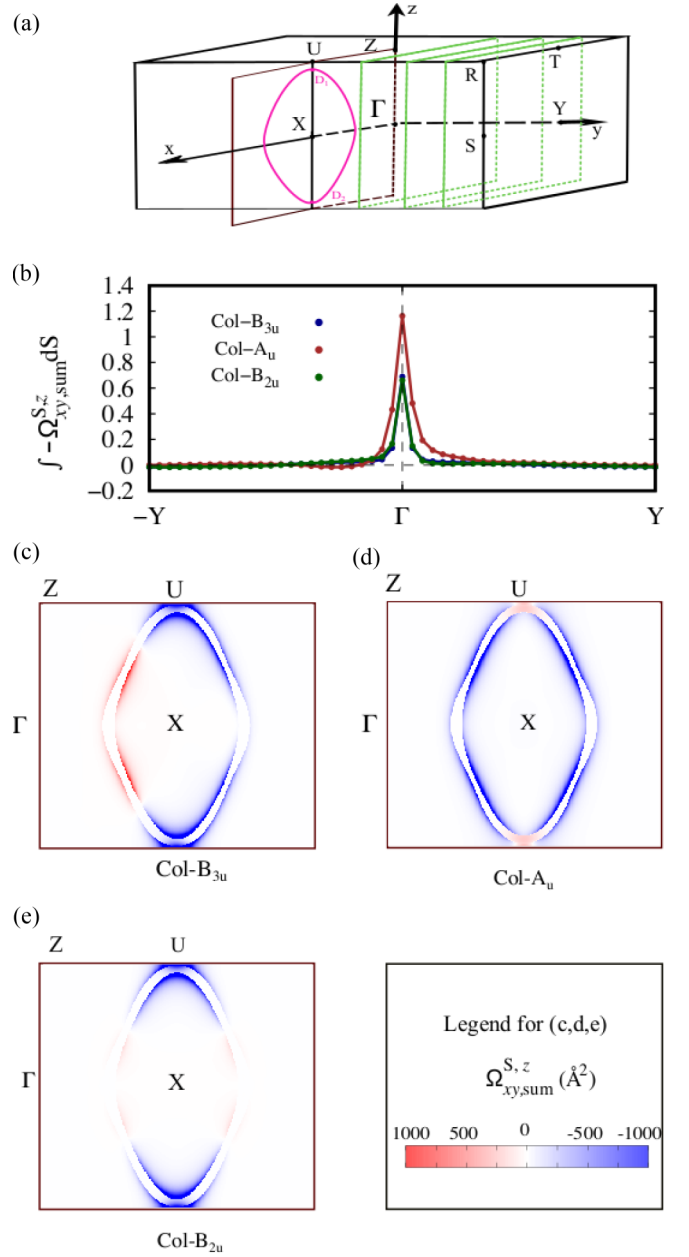
FIG. 6. (a) Nodal line (pink) in the (010) plane including Γ in the Col-B_{3u}, Col-A_u, and Col-B_{2u} magnetic structures without SOC. (b) The spin Berry curvature after taking the band summation is integrated on the (010) planes for the Col-B_{3u} (dark-blue), Col-A_u (brown), and Col-B_{2u} (dark-green) structure with SOC with its center changing from $-Y$ to Γ, and to Y [illustrated as green rectangles in (a)]. (c)–(e) The spin Berry curvature when the SOC is included for the Col-B_{3u}, Col-A_u, and Col-B_{2u} magnetic structures, respectively.

curvature along the high-symmetry lines for the different magnitudes of external magnetic fields H_x in Fig. 7(d). The magnetic fields strongly reduce the intensity of the spin Berry curvature component, especially around the U point of the BZ, at which the Dirac points are present around, against the small change in the band structure [see Fig. 7(d)] and suppress the SHC as a result [see Fig. 7(c)].
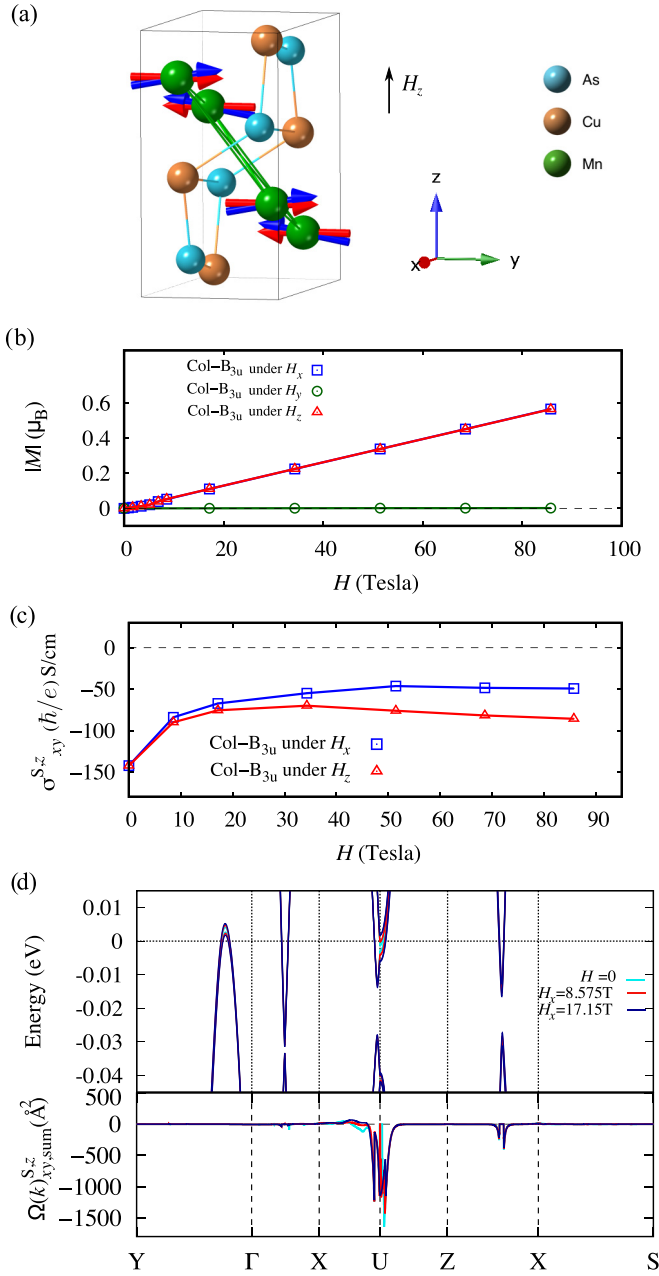
(a)

(b)

(c)

(d)

FIG. 7. (a) Illustration of the change of the local magnetic moment under H_z for the Col-B_{3u} magnetic structure. The red vectors show magnetic moments in the ground state, and the blue vectors show canted magnetic moments under H_z. (b) Magnetization under the magnetic fields H_x, H_y, H_z in the Col-B_{3u} magnetic structure. (c) The SHC $\sigma_{xy}^{S,z}$ under H_x and H_z in the Col-B_{3u} magnetic structure. (d) Change of the electronic band structure and spin Berry curvature under the external magnetic fields along high-symmetry lines.

D. Anomalous Hall effect under external magnetic fields

In the collinear-AFM states of CuMnAs, the preserved TP symmetry forbids the AHC to be finite. Meanwhile, we here show that the intrinsic AHC component can be developed significantly with the applied magnetic fields due to the local intensive contribution of the Berry curvature for the Bloch states related to the topological bands. The result in Fig. 8(a) shows the development of the AHC under different directions
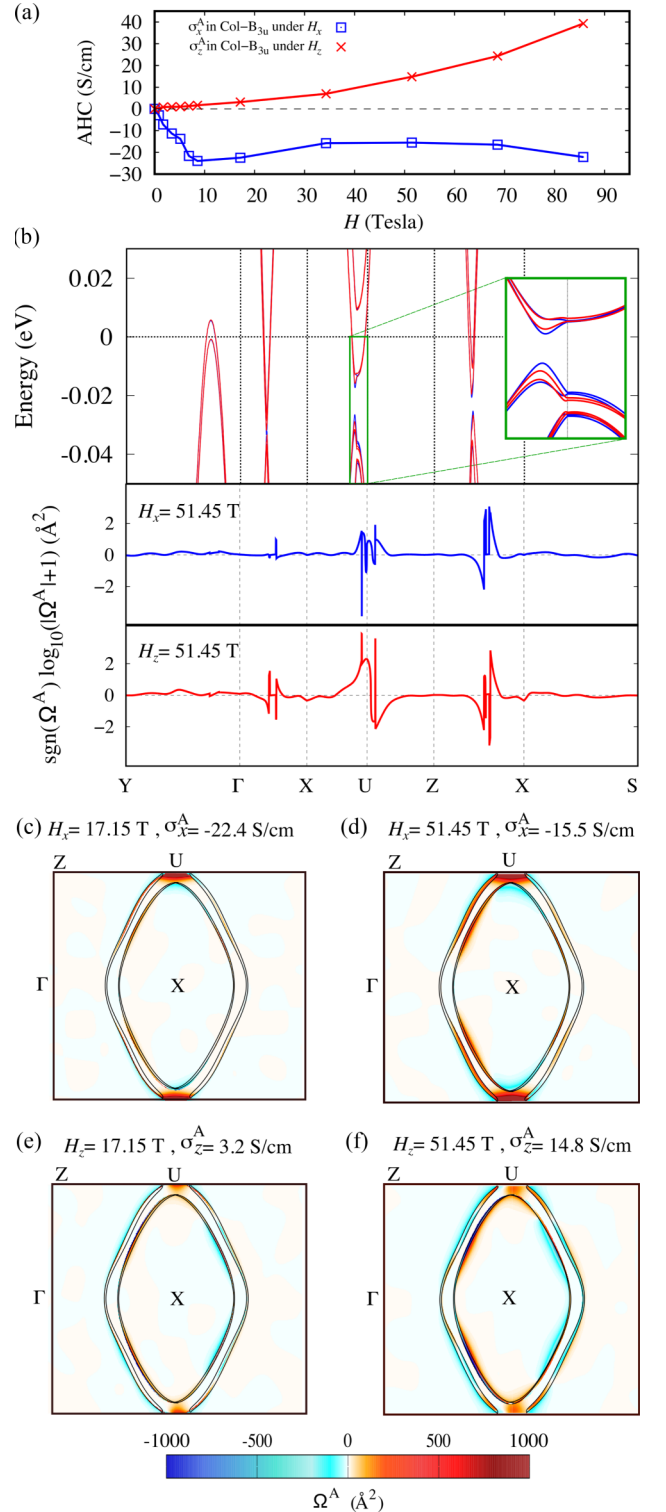

(a)

(b)

(c) $H_x = 17.15$ T , $\sigma_x^A = -22.4$ S/cm   (d) $H_x = 51.45$ T , $\sigma_x^A = -15.5$ S/cm

(e) $H_z = 17.15$ T , $\sigma_z^A = 3.2$ S/cm   (f) $H_z = 51.45$ T , $\sigma_z^A = 14.8$ S/cm

FIG. 8. (a) The AHC $\sigma_x^A = \sigma_{yz}^A$ and $\sigma_z^A = \sigma_{xy}^A$ under H_x and H_z in the Col-B_{3u} structure. (b) The electronic structure along high-symmetry lines, and the corresponding Berry curvature Ω^A indicating $\Omega_x = \Omega_{\text{sum},yz}^A$ or $\Omega_z = \Omega_{\text{sum},xy}^A$ in the logarithm base 10 scale, $\text{sgn}(\Omega^A) \log_{10}(|\Omega^A| + 1)$, under magnetic fields H_x (blue) and H_z (red) of 51.45 T. Here, $\text{sgn}(x)$ is the sign function, i.e., $\text{sgn}(x) = -1$ if $x < 0$, $\text{sgn}(x) = 0$ if $x = 0$, and $\text{sgn}(x) = 1$ if $x > 0$. (c)–(f) Berry curvature in the (010) plane containing Γ for $H_x = 17.15$ T, $H_x = 51.45$ T, $H_z = 17.15$ T, $H_z = 51.45$ T, respectively, with the black lines indicating the Fermi surface.
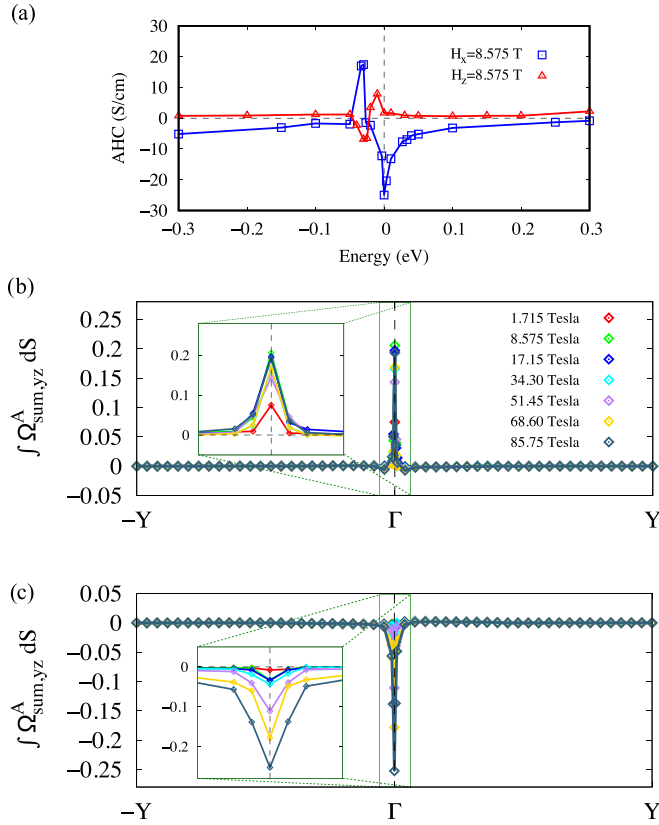
FIG. 9. (a) The AHC as a function of the energy around the Fermi energy in the case of applied magnetic fields 8.575 T along the x axis and z axis in the Col-B_{3u} structure. The Berry curvature integrated on the (010) plane with its center changing from $-Y$ to Γ, and to Y for the Col-B_{3u} structure with SOC under different (b) H_x and (c) H_z.

of the applied magnetic fields H_x and H_z which cause the linear development of the magnetization in the Col-B_{3u} structure in Fig. 7(b). Under the magnetic field along the x axis, the magnitude of AHC σ_x^A increases from zero to 27 S/cm at H_x of about 8.575 T and shows only a weak change above the fields. Meanwhile, the AHC σ_z^A increases monotonically with increasing magnetic field along the z axis.

We show the electronic band structure and corresponding Berry curvature along the high-symmetry lines in the case of the applied magnetic fields of 51.45 T along the x and z axis in Fig. 8(b). As shown in Fig. 8(b), the Berry curvature around the U point exhibits a large difference for the different directions of the applied magnetic fields against the small change in the band structure. The difference can be seen more clearly for the distribution of the Berry curvature in the (010) plane including the Γ point for different directions as plotted in Figs. 8(c)–8(f). The figure shows the stronger intensity of the Berry curvature around the U point under H_x magnetic fields than that under H_z fields while the small Berry curvature under H_z fields spreads more around the gapped nodal lines than that under H_x fields. Since the local peaky Berry curvature can change drastically with the small change in the energy bands and a widely spread small Berry curvature provides a more gradual change in the contribution to the AHC, the difference in the development of

TABLE VII. The dependence of AHC on the k-mesh and adaptive mesh (Adapt.) at peaks of AHC values in the Col-B_{3u} structure in Fig. 9(a).

(a) Under $H_x = 8.575$ T		
	σ_x^A(S/cm)	
k mesh (Adapt.)	$E = -0.03$ eV	$E = 0$ eV
$180 \times 280 \times 180$ ($5 \times 5 \times 5$)	16.9676	-23.9518
$180 \times 280 \times 180$ ($7 \times 7 \times 7$)	17.7158	-23.9188
$200 \times 300 \times 200$ ($7 \times 7 \times 7$)	17.4178	-24.9715
(b) Under $H_z = 8.575$ T		
	σ_z^A (S/cm)	
k mesh (Adapt.)	$E = -0.03$ eV	$E = -0.01$ eV
$180 \times 280 \times 180$ ($5 \times 5 \times 5$)	5.8248	7.5697
$180 \times 280 \times 180$ ($7 \times 7 \times 7$)	-6.6037	7.4908
$200 \times 300 \times 200$ ($7 \times 7 \times 7$)	-6.8678	7.8558

AHC for different magnetic field directions can be explained by the different origin of the Berry curvature, as shown in Figs. 8(c)–8(f).

We show the AHC value as a function of chemical potential in the Col-B_{3u} structure at an external magnetic field of 8.575 T in Fig. 9(a). The result shows the drastic change of magnitude and sign of AHC values around the energy of the gapped out nodal line, which is about from 0 to 30 meV below the Fermi energy. The rapid change implies the possible change in the AHC value via chemical doping and partly helps us to realize the origin of the AHC possible from the gapped nodal line. We increase the k mesh to check the convergence around the region with the rapid change shown in Table VII. To see where the largest contribution of the Berry curvature is to the AHC, we estimated the sum of the Berry curvature in (010) planes with its center changing from $-Y$ to Γ and to Y for the different intensity values of H_x and H_z in the Col-B_{3u} structure. The result in Figs. 9(b) and 9(c) shows that the largest summation belongs to the (010) plane including Γ, which contains the gapped out Dirac nodal line by SOC. The microscopic mechanism leading to significant anomalous components of the Hall effect predicted for the AFM CuMnAs is therefore concluded to be the further lifting of band degeneracy under external magnetic fields for the Bloch states generated with the splitting of nodal lines by SOC near the Fermi energy.

V. CONCLUSIONS

In summary, we investigated the influence of topological bands in macroscopic transport phenomena, SHE and AHE, in orthorhombic CuMnAs. We provided a symmetry analysis for these transport phenomena and magnetic structures in the crystal structure. The collinear-AFM states in CuMnAs form Dirac nodal lines in the energy bands near the Fermi energy in the absence of SOC and the nodal lines generate a large SHC with lifting degeneracies by SOC. The change of the SHC from the antisymmetric tensor components in the nonmagnetic state to anisotropic ones in the AFM states enables us to manipulate the spin current by controlling mag-

netism, and is expected to be applicable as spintronics devices [15,16,42–53].

An experimentally observed collinear-AFM state referred to as the Col-B_{3u} structure, in which the local magnetic moments are aligned along the b axis, is investigated with the effect of applied magnetic fields. Applied magnetic fields cause a drastic change in the SHC and AHC with the local contribution from the Bloch states around the nodal lines opening the gap with SOC through further lifting of the band degeneracy due to TP symmetry breaking, against the simple linear development of the magnetization.

The rapid chemical potential dependence in the SHC and AHC leads to the possibility to manipulate these transport phenomena via chemical doping in CuMnAs. The SHC and AHC in the collinear-AFM state thus can pave a way to control these phenomena in the fields of spintronics as well

as to investigate the transport phenomena for further AFM materials.

[1] N. Nagaosa, J. Sinova, S. Onoda, A. H. MacDonald, and N. P. Ong, Rev. Mod. Phys. **82**, 1539 (2010).

[2] D. Xiao, M. C. Chang, and Q. Niu, Rev. Mod. Phys. **82**, 1959 (2010).

[3] V. Baltz, A. Manchon, M. Tsoi, T. Moriyama, T. Ono, and Y. Tserkovnyak, Rev. Mod. Phys. **90**, 015005 (2018).

[4] S. Nakatsuji, N. Kiyohara, and T. Higo, Nature (London) **527**, 212 (2015).

[5] N. Kiyohara, T. Tomita, and S. Nakatsuji, Phys. Rev. Appl. **5**, 064009 (2016).

[6] H. Chen, Q. Niu, and A. H. MacDonald, Phys. Rev. Lett. **112**, 017205 (2014).

[7] J. Kübler and C. Felser, Europhys. Lett. **108**, 67001 (2014).

[8] V. T. N. Huyen, M.-T. Suzuki, K. Yamauchi, and T. Oguchi, Phys. Rev. B **100**, 094426 (2019).

[9] A. Sakai, Y. P. Mizuta, A. A. Nugroho, R. Sihombing, T. Koretsune, M.-T. Suzuki, N. Takemori, R. Ishii, D. Nishio-Hamane, R. Arita, P. Goswami, and S. Nakatsuji, Nat. Phys. **14**, 1119 (2018).

[10] S. N. Guin, P. Vir, Y. Zhang, N. Kumar, S. J. Watzman, C. Fu, E. Liu, K. Manna, W. Schnelle, J. Gooth, C. Shekhar, Y. Sun, and C. Felser, Adv. Mater. **31**, 1806622 (2019).

[11] S. Minami, F. Ishii, M. Hirayama, T. Nomoto, T. Koretsune, and R. Arita, Phys. Rev. B **102**, 205128 (2020).

[12] Y. Yanagi, J. Ikeda, K. Fujiwara, K. Nomura, A. Tsukazaki, and M.-T. Suzuki, Phys. Rev. B **103**, 205112 (2021).

[13] T. Tanaka, H. Kontani, M. Naito, T. Naito, D. S. Hirashima, K. Yamada, and J. Inoue, Phys. Rev. B **77**, 165117 (2008).

[14] F. Freimuth, S. Blügel, and Y. Mokrousov, Phys. Rev. Lett. **105**, 246602 (2010).

[15] W. Zhang, M. B. Jungfleisch, W. Jiang, J. E. Pearson, A. Hoffmann, F. Freimuth, and Y. Mokrousov, Phys. Rev. Lett. **113**, 196602 (2014).

[16] Y. Yen and G.-Y. Guo, Phys. Rev. B **101**, 064430 (2020).

[17] P. Tang, Q. Zhou, G. Xu, and S.-C. Zhang, Nat. Phys. **12**, 1100 (2016).

[18] L. Šmejkal, J. Železný, J. Sinova, and T. Jungwirth, Phys. Rev. Lett. **118**, 106402 (2017).

[19] F. Máca, J. Mašek, O. Stelmakhovych, X. Martí, H. Reichlová, K. Uhlířová, P. Beran, P. Wadley, V. Novák, and T. Jungwirth, J. Magn. Magn. Mater. **324**, 1606 (2012).

[20] E. Emmanouilidou, H. Cao, P. Tang, X. Gui, C. Hu, B. Shen, J. Wu, S.-C. Zhang, W. Xie, and N. Ni, Phys. Rev. B **96**, 224405 (2017).

[21] M. V. Berry, Proc. R. Soc. London, Ser. A **392**, 45 (1984).

[22] F. D. M. Haldane, Phys. Rev. Lett. **93**, 206602 (2004).

[23] D. J. Thouless, M. Kohmoto, M. P. Nightingale, and M. denNijs, Phys. Rev. Lett. **49**, 405 (1982).

[24] X. Wang, J. R. Yates, I. Souza, and D. Vanderbilt, Phys. Rev. B **74**, 195118 (2006).

[25] P. Giannozzi, S. Baroni, N. Bonini, M. Calandra, R. Car, C. Cavazzoni, D. Ceresoli, G. L. Chiarotti, M. Cococcioni, I. Dabo, A. D. Corso, S. de Gironcoli, S. Fabris, G. Fratesi, R. Gebauer, U. Gerstmann, C. Gougoussis, A. Kokalj, M. Lazzeri, L. M. Samos *et al.*, J. Phys.: Condens. Matter **21**, 395502 (2009).

[26] J. P. Perdew, K. Burke, and M. Ernzerhof, Phys. Rev. Lett. **77**, 3865 (1996).

[27] P. E. Blöchl, Phys. Rev. B **50**, 17953 (1994).

[28] G. Kresse and D. Joubert, Phys. Rev. B **59**, 1758 (1999).

[29] A. D. Corso, Comput. Mater. Sci. **95**, 337 (2014).

[30] M. B. Nardelli, F. T. Cerasoli, M. Costa, S Curtarolo, R. De Gennaro, M. Fornari, L. Liyanage, A. R. Supka, and H. Wang, Comput. Mater. Sci. **143**, 462 (2018).

[31] J. K. Dewhurst, S. Sharma, L. Nordström, F. Cricchio, O. Grånäs, H. Gross, C. Ambrosch-Draxl, C. Persson, F. Bultmark, C. Brouder *et al.*, http://elk.sourceforge.net/.

[32] A. A. Mostofi, J. R. Yates, G. Pizzi, Y. S. Lee, I. Souza, D. Vanderbilt, and N. Marzari, Comput. Phys. Commun. **185**, 2309 (2014).

[33] N. Marzari, A. A. Mostofi, J. R. Yates, I. Souza, and D. Vanderbilt, Rev. Mod. Phys. **84**, 1419 (2012).

[34] Y. Yao, L. Kleinman, A. H. MacDonald, J. Sinova, T. Jungwirth, D.-S. Wang, E. Wang, and Q. Niu, Phys. Rev. Lett. **92**, 037204 (2004).

[35] M.-T. Suzuki, T. Nomoto, R. Arita, Y. Yanagi, S. Hayami, and H. Kusunose, Phys. Rev. B **99**, 174407 (2019).

[36] H. Grimmer, Acta Cryst. **49**, 763 (1993).

[37] D. Gosálbez-Martínez, I. Souza, and D. Vanderbilt, Phys. Rev. B **92**, 085138 (2015).

[38] M.-T. Suzuki, T. Koretsune, M. Ochi, and R. Arita, Phys. Rev. B **95**, 094406 (2017).

[39] M. Seemann, D. Ködderitzsch, S. Wimmer, and H. Ebert, Phys. Rev. B **92**, 155138 (2015).

[40] M.-T. Huebsch, T. Nomoto, M.-T. Suzuki, and R. Arita, Phys. Rev. X **11**, 011031 (2021).

[41] L. He, F. Liu, G. Hautier, M. J. T. Oliveira, M. A. L. Marques, F. D. Vila, J. J. Rehr, G.-M. Rignanese, and A. Zhou, Phys. Rev. B **89**, 064305 (2014).

[42] J. Železný, Y. Zhang, C. Felser, and B. Yan, Phys. Rev. Lett. **119**, 187204 (2017).

[43] Y. Zhang, J. Železný, Y. Sun, J. van den Brink, and B. Yan, New J. Phys. **20**, 073028 (2018).

[44] M. Kimata, H. Chen, K. Kondou, S. Sugimoto, P. K. Muduli, M. Ikhlas, Y. Omori, T. Tomita, A. H. MacDonald, S. Nakatsuji, and Y. Otani, Nature (London) **565**, 627 (2019).

[45] M. Naka, S. Hayami, H. Kusunose, Y. Yanagi, Y. Motome, and H. Seo, Nat. Commun. **10**, 4305 (2019).

[46] K.-H. Ahn, A. Hariki, K.-W. Lee, and J. Kuneš, Phys. Rev. B **99**, 184432 (2019).

[47] S. Hayami, Y. Yanagi, and H. Kusunose, J. Phys. Soc. Jpn. **88**, 123702 (2019).

[48] S. Hayami, Y. Yanagi, and H. Kusunose, Phys. Rev. B **101**, 220403(R) (2020).

[49] S. Hayami, Y. Yanagi, and H. Kusunose, Phys. Rev. B **102**, 144441 (2020).

[50] A. Mook, R. R. Neumann, A. Johansson, J. Henk, and I. Mertig, Phys. Rev. Research **2**, 023065 (2020).

[51] L.-D. Yuan, Z. Wang, J.-W. Luo, E. I. Rashba, and A. Zunger, Phys. Rev. B **102**, 014422 (2020).

[52] M. Naka, Y. Motome, and H. Seo, Phys. Rev. B **103**, 125114 (2021).

[53] R. González-Hernández, L. Šmejkal, K. Výborný, Y. Yahagi, J. Sinova, T. Jungwirth, and J. Železný, Phys. Rev. Lett. **126**, 127701 (2021).